Received: 8 January 2024 | Revised: 7 May 2024 | Accepted: 20 May 2024

DOI: 10.1111/ijac.14824

International Journal of Applied Ceramic Technology

RESEARCH ARTICLE

Application of Johnson's approximation in finite element modeling for electric field-dependent materials

Rassell C. D'Silva Green[1] | **Graham Dale**[2] | **Garry McLaughlin**[2] | **Maureen Strawhorne**[2] | **Derek C. Sinclair**[1] | **Julian S. Dean**[1]

[1]Department of Material Science & Engineering, University of Sheffield, Sheffield, UK

[2]Kyocera AVX Components Ltd, Coleraine, Londonderry, UK

Correspondence
Julian S. Dean, Department of Material Science & Engineering, University of Sheffield, Sheffield, UK.
Email: j.dean@sheffield.ac.uk

Abstract

Johnson's approximation is implemented in a finite element code to simulate the electric field dependence of a core–shell microstructure material. We show how the microstructure, based here on a 50:50 volume fraction, influences the measured effective permittivity as a function of applied voltage. Using a Johnson's parameter of $\beta = 1.0 \times 10^{10}$ Vm^5/C^3, verified from commercial $BaTiO_3$-based multilayer ceramic capacitors (MLCC), we show how the microstructure and the difference in core and shell conductivities alter the local fields generated and how this influences the voltage dependence of the effective permittivity. Systems that comprise a conductive core-like material surrounded by a resistive shell experience little or modest voltage dependence due to the shell material providing shielding to large electric fields within the cores. Conversely, if the core material is more resistive than the shell material, substantial voltage dependence occurs with simulations showing over a 50% decrease in the effective permittivity. These simulations give improved understanding of voltage dependence and provide a method to help guide the design of future materials for MLCCs with improved performance.

KEYWORDS

barium titanate, ferroelectricity/ferroelectric, finite element analysis, materials, multilayer ceramic capacitor

1 | INTRODUCTION

Multilayer ceramic capacitors (MLCCs) are among the most mass-produced devices with over 3.5 trillion units being manufactured per year,[1] with the value of the MLCC global market expected to reach over 14 billion USD by 2024.[1] They are used in small- and large-scale applications varying from smartphones, and automobiles to uses in wireless communication.[2,3] With the rapid growth of 5G and electric vehicles, capacitors need to evolve toward higher frequencies (>MHz), higher voltages (>1 kV), higher breakdown strengths (>100 kV/cm), and higher temperatures (>400°C for some space exploration applications).[4] In automotive applications, due to their use in under-the-hood applications, the materials are required to operate at temperature ranges of −55 to 150°C, and

voltages over 240 V,[4] while maintaining their small size and high thermally stable capacitance. A capacitor which meets these requirements is classified as an X8R ±15%.

MLCCs consist of several layers of a ceramic material sandwiched between two metal electrodes where the capacitance of an MLCC is calculated by:

$$C = \frac{\epsilon_r \epsilon_0 A}{d} \times (n) \quad (1)$$

Here, capacitance, C is typically measured in pF or μF, ϵ_r is its relative permittivity, and ϵ_0 is the permittivity of free space (8.8542×10^{-12} F/m). The geometry is defined as the surface area of the electrode given by A, d is the distance between the electrodes, and n is the number of active ceramic layers between electrodes, which can be several hundred in typical commercial MLCCs.

The three variables in Equation (1) provide possible ways to improve the capacitance of an MLCC. The first is to increase the permittivity of the ceramic, the second is to reduce the distance between the electrodes, and the third is to increase the surface area of the plates. Each of these methods has its benefits and implications. Although increasing the surface area of the electrode is possible, this would increase the footprint of the device. Since MLCCs are usually size limited due to space available on circuit boards, this is not a viable solution.

Although the permittivity of the material could be improved, there are limitations on which materials could achieve this. Ferroelectric barium titanate ($BaTiO_3$) is the base ceramic material of choice as it possesses a high intrinsic room temperature permittivity (1000–7000[5]) and is compatible with current manufacturing techniques.[6] However, the permittivity is highly dependent on the temperature and needs modification to meet current requirements.[7] A measurement of the temperature dependence of ferroelectrics is via the temperature coefficient of capacitance (TCC), which is calculated by the formula:

$$\text{TCC}\% = \frac{\epsilon_T - \epsilon_{25}}{\epsilon_{25}} \times 100 \quad (2)$$

where ϵ_{25} is the permittivity at room temperature and ϵ_T is the permittivity at the reference temperature. One way to increase temperature stability is via chemical doping of $BaTiO_3$ to form a core–shell microstructure.[8] Undoped $BaTiO_3$ has a sharp peak in permittivity at its Curie temperature as it undergoes a phase transition from a tetragonal to a cubic crystal structure. Through chemical modifications via different dopants,[9,10] a dopant-rich shell can be formed, which typically has a much broader transition range at lower temperatures than the Curie temperature of undoped $BaTiO_3$. The combination of the core and shell microstructure extends the temperature range over which a capacitor can operate, allowing it to meet the required specification that undoped $BaTiO_3$ could not achieve. In addition, other properties such as processing conditions,[11] layer thicknesses,[12] and grain size[13] allow the TCC to be controlled to meet industrial specifications. Determining the optimal volume ratio for the application, however, can involve a time-consuming iterative process to arrive at the appropriate formulation and processing conditions.[4]

An efficient method to increase capacitance is to reduce the distance between the electrodes. This provides two benefits: it gives the possibility of smaller devices and increased capacitance; however, the electric field is increased as the dielectric thickness is decreased, given by:

$$E_G = \frac{V}{d} \quad (3)$$

where V is the applied voltage across the electrodes and d is the distance between the electrodes. As Equation (3) only considers the global properties of the system, we shall refer to this value as the global electric field E_G to distinguish it from the variations of the local electric fields produced inside the material. As d is reduced to a few microns, the strength of the global electric field can increase to over 1 MV/m for an applied voltage of 1 V. At room temperature, the breakdown voltage of $BaTiO_3$ is around 3 MV/m.[14] The lifetime of these components can therefore be compromised in higher voltage applications.

There has been extensive research into improving TCC, however, an often-overlooked aspect in optimizing these materials is the voltage coefficient of capacitance (VCC). For some materials, the application of high electric fields can create a reduction in the permittivity along with a shift of the Curie peak toward a higher temperature.[15] The macroscopic tunability of the capacitance can be attributed to several bias field-induced modifications at various length scales from the unit cell polarization (intrinsic), polar nanoregions, domain relaxation, grain boundaries, and interphases.[16,17] These occur at lengths scales from nano- to micro-meter and can depend on temperature, frequency, crystal symmetry, and ceramic microstructure. One method of approximating the macroscopic tunability is to use the empirical Johnson's approximation.[18,19] This is based on the Landau–Devonshire phenomenological theory,[17] which has been used successfully to fit the tunability of various materials.[18] Although the Johnson's approximation is limited in explaining the hysteretic behavior of the dielectric permittivity below the Curie temperature, it has been shown to work well in predicting the voltage dependence of $BaTiO_3$-based materials.[18,20,21] Furthermore, it has also been shown that the weak field

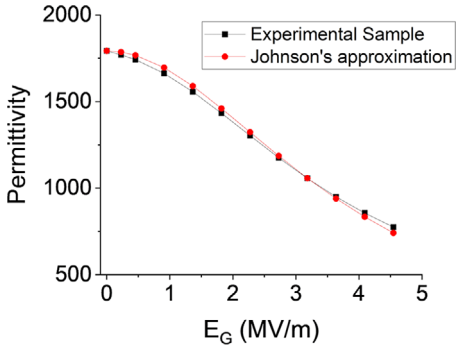

FIGURE 1 Voltage coefficient of capacitance (VCC) data for a commercial $BaTiO_3$-based multilayer ceramic capacitor measured at 25°C (black) at a frequency of 100 kHz and fitted with Equation (2) (in red) to extract the Johnson parameter β. In this case, the value extracted is $\beta = .67 \times 10^{10}$ Vm^5/C^3.

approximation model, based on the Gibbs free energy, also provides good agreement with Johnson's equation.[21]

The nonlinear field dependence of the permittivity can be described by the Johnson's equation which has been used successfully to fit the variation of permittivity with electric field data for $BaTiO_3$.[19,21,22]

$$\epsilon_r(E) = \frac{\epsilon_r(0)}{\left(1 + 3\beta(\epsilon_0\epsilon_r(0))^3 E^2\right)^{\frac{1}{3}}} \tag{4}$$

Here, $\epsilon_r(E)$ is the modified relative permittivity measured when an electric field strength E (V/m) is generated in the material. The relative permittivity in the absence of an electric field is given by $\epsilon_r(0)$ and the variable β is an anharmonic coefficient also known as Johnson's parameter and represents the ferroelectric nonlinearity of the material. This can be estimated by fitting the observed permittivity drop with increasing voltage[22] as shown in Figure 1. By fitting experimental data using this equation, depending on the composition, the value of β can be temperature dependent and vary by an order of magnitude.[18]

In Figure 1, experimental data from a commercial $BaTiO_3$-based MLCC are measured as a function of E_G. In this case, the data were generated by changing the applied voltage on the same thickness of dielectric (i.e., changing V, but maintaining d), however, using Equation (3), as the permittivity change is generated by the applied E_G (i.e., the ratio of V/d) this could also give insight into what can happen if the applied voltage is maintained but the dielectric thickness, d is reduced. Fitting Figure 1 with Equation (4), Johnson's parameter can be extracted, in this case, $\beta = .67 \times 10^{10}$ Vm^5/C^3 at a temperature of 25°C. Within the literature, β values are reported in the order of 10^{10} and up to 10^{12} Vm^5/C^3,[23,24] matching well with our results here. There are limitations to the accuracy of Johnson's approximation. For example, when the grain size is reduced to nanometers, there is a known decrease in the permittivity of $BaTiO_3$. This has been attributed to increasing electrical inhomogeneity as the grain size is reduced.[4] Some approaches to tackle this issue involve using a material-dependent exponent[25] or utilizing a coefficient dependent on the microstructure.[26] Typically, VCC data are not measured for nanostructured ceramics as it requires measuring permittivity at low thicknesses, which leads to the generation of extremely high electric fields.[4,27]

There has been work on studying this effect through modeling. Padurariu et al.[14] developed a finite element model (FEM) to mimic a two dimensional grain structure consisting of nonlinear ferroelectric grain cores with paraelectric grain boundaries. The model consisted of multiple grains with varying sizes. For large grain sizes, they showed there is a negligible difference between the global and local electric fields. With decreasing grain size there is a reduction in the local electric field in the core leading to an increase in the local field inhomogeneity. Due to the presence of this inhomogeneity, Johnson's approximation applied globally to the system would not be sufficient to describe the behavior of this system as it uses the global field. This can be resolved by using the local field values generated to determine the local changes in permittivity. Although their method was able to describe the effective field permittivity using the local field evolution and local permittivity, a limitation of their method is that it is confined to a two-dimensional model.

In this article, we implement Johnson's approximation into our in-house impedance software ElCer.[28] This provides the ability to simulate the local electric fields arising from the microstructure and variation in core and shell material properties, which we can represent in a full three-demensional model. This can be used to help understand how microstructural features can influence the field-dependent response of materials used in MLCCs.

2 | METHODOLOGY

To simulate how Johnson's approximation influences the material's electric response under an applied electric field, we first create the desired microstructure. Figure 2 highlights the procedure on a simple series layered model, Figure 2A, noting that this procedure is the same for any microstructure such as a core–shell or a collection of grains. The model is drawn, in this case as a 10 μm cube encompassing two layers, and discretized into elements using Gmsh,[29] where each element is individually assigned the material permittivity, conductivity, and Johnson's parameter. Materials which are field dependent are

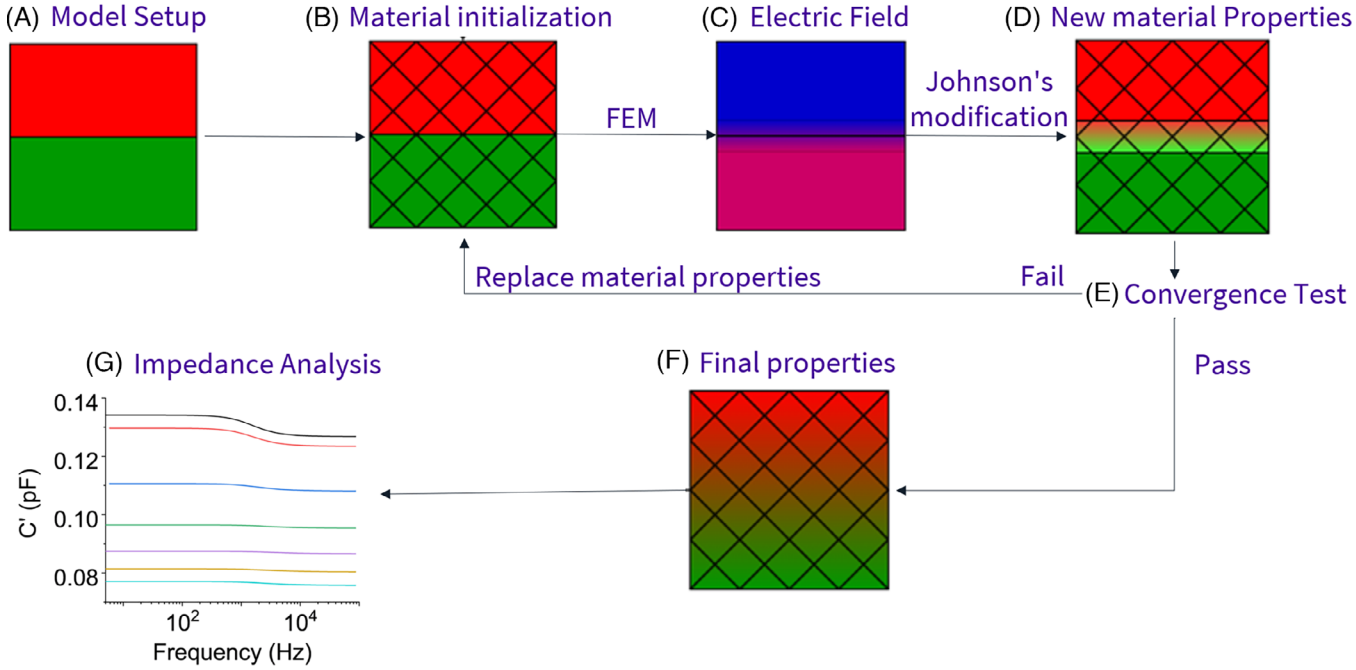

FIGURE 2 Schematic showing the coding process using a simple layered model as an example. The initial model (A) and the materials initialized (B). ElCer is first used to simulate the electric field (C). Johnson's equation is then used to modify the material properties as shown in (D). Once the system has passed the test for convergence (E) we use the final properties (F) to simulate the impedance response. The capacitance formalism *C*' (G) is then used to extract capacitance at fixed frequencies.

set to Johnson's parameter of $\beta = 1.0 \times 10^{10}$ Vm^5/C^3, chosen as it falls within the accepted known range for $BaTiO_3$[19,20] and close to our experimentally extracted value. For materials which experience non-field dependence (NFD), we set $\beta = 0$. We finally apply a voltage of 110 V across the model as explained in Figure 2B, which, using Equation (3), generates an E_G of 11 MV/m over the model.

Using our in-house impedance software ElCer,[23] we first simulate the local electric field distribution within the microstructure as shown in Figure 2C. We assume the material properties to be isotropic and linear and that any inductive effects are negligible when compared with the capacitive behavior. ElCer uses a time-domain finite element method (TDFEM) based on Maxwell's equations to calculate the electric potential as a function of space and time. This permits the current density to be calculated by integrating over the whole sample, and thus, in turn, allows simulation of the electrical response of the electroceramic. We use Dirichlet boundary conditions at the electrode–air interface to fix the electric potential. Furthermore, we assume that the displacement currents across the free surface of the material are zero by implementing a Neumann boundary condition at those regions. We note that although other thermal and electromechanical effects such as thermoelectricity or piezoelectricity are present in $BaTiO_3$ for simplicity we do not consider these in the model but they could be explored in the future.

Depending on the microstructure and material properties, this could be significantly higher or lower than the global electric field. These local values are then weighted onto the centroid of each element and converted to a change of local permittivity using Johnson's equation (Equation 4) as shown in Figure 2D. The process is repeated until convergence is achieved, which we set at a value of less than .1% difference between subsequent runs, Figure 2E. At convergence, a final model is generated (Figure 2F) and an impedance spectrum generated for analysis as shown in Figure 2G. This entire process can be repeated for higher voltages to understand how the materials respond at different electric field strengths. Although we have controlled the voltage to generate large electric field strengths across the materials, from Equation (3), the larger electric fields can also be used to represent a change in the multilayer thickness with a constant voltage.

The simulation of the impedance spectra provides a method of identifying the response of the constituent materials.[30] Here, we focus on the analysis of the *C*' spectra (real part of capacitance vs. frequency), Figure 2G, where the effective capacitance at various fixed frequencies can be extracted and converted to permittivity using a geometric factor.

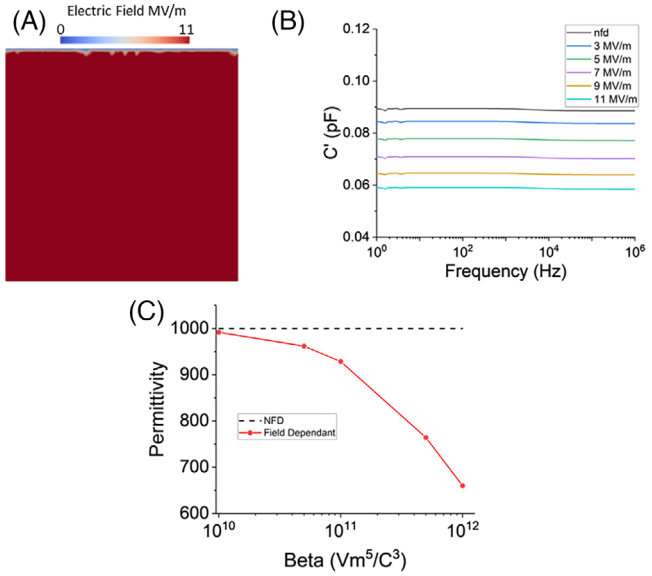

FIGURE 3 A simple uniform material under a potential difference of 110 V. (A) The electric field distribution within the material, (B) *C*' spectroscopic plots for the simple cubic model with increasing electric field, and (C) the change in permittivity as the Johnson's parameter, β, is increased for the simple cubic model. The dashed line indicates the non-field dependent (NFD) model.

To verify this method, we simulate the impedance response of a simple, electrically homogenous cube as shown in Figure 3. The model consists of a cube with a side length of 10 μm, the initial permittivity of ϵ_r = 1000 and conductivity of $\sigma = 100$ μS/m. This cube is discretized into ~165k tetrahedral elements and the local electric field distribution is simulated. As the cube is made from a single material, a homogeneous response is generated, as shown in Figure 3A. The resulting *C*' spectra of this system are shown in Figure 3B.

As applying zero voltage across the material is equivalent to the material being assigned $\beta = 0$ Vm^5/C^3, for clarity we refer to these simulations throughout the article as the non-field dependent (NFD) case. Solving and plotting spectra in the *C*' formalism generate a single plateau with capacitance of .089 pF. As the voltage is increased, the *C*' plateau decreases uniformly, as seen in Figure 3B. This continues up to the maximum applied global field of 11 MV/m, where the capacitance drops to .059 pF. As Johnson's parameter β range can be a few orders of magnitude, we simulate various values within the literature range as shown in Figure 3C and by converting the capacitance, *C*' to permittivity using the geometrical factor. As shown, the drop in permittivity from the NFD of $\epsilon_r = 1000$ to below 700 for global fields of 11 MV/m when $\beta = 1 \times 10^{10}$ Vm^5/C^3 is used. It should be noted that all solved values here are consistent with Equation (4) as the global and local fields are equivalent.

TABLE 1 The assigned material properties used for Cases I–VI for the core–shell models.

Case	Core/shell	Permittivity	Conductivity (μS/m)
I/IV	Shell	1000	100
	Core	2000	100
II/V	Shell	1000	100
	Core	2000	.1
III/VI	Shell	1000	.1
	Core	2000	100

To increase realism in the physical microstructure, we now create a core and shell structure which can arise in doped $BaTiO_3$ materials and commercial MLCCs.[7,31] We set the core–shell volume ratio as a 50–50 ratio and the total side length of the system as 10 μm, as shown in Figure 4A. To ensure the results are not influenced by surface effects, we use 27 identical core–shell cubes set in a 3 × 3 × 3 array and extract the results from only the central grain. In this first study, the shell and core were both assigned a permittivity of $\epsilon_r = 1000$ and a conductivity $\sigma = 100$ μS/m. Typical shell materials have a significantly lower sensitivity to field effects[32,33] and so we set the core to have Johnson's parameter of $\beta = 1 \times 10^{10}$ Vm^5/C^3 but assign the shell to be NFD (i.e., $\beta = 0$ Vm^5/C^3).

Figure 4B shows a combined image of the electric field and permittivity distribution after convergence. The left side of Figure 4B highlights the electric field distribution in the core–shell model (left). As both core and shell have the same conductivity, as in the previous simple cube case, the response at NFD is a homogenous field response of 11 MV/m through both materials. However, as the core experiences the electric field its permittivity is reduced as shown in Figure 4B (right). This generates a 33.7% drop in the capacitance of the material from ~.089 pF to .059 pF when a global field of 11 MV/m is applied, Figure 4C. The simulated *C*' spectra begin to display two distinct plateaus at higher fields, highlighting a significant change in the core material whereas the shell remains unchanged. This drop becomes linear as shown in Figure 4D and the trend reproduces that observed experimentally in Figure 1.

3 | RESULTS AND DISCUSSION

In the above methodology, the core and shell materials were set to have the same properties but this is unlikely and unrealistic due to known compositional changes of the core and shell materials in $BaTiO_3$-based MLCCs. We therefore extend our study to six different configurations, as shown in Table 1. In each study, the core and shell properties are varied so regions have either a

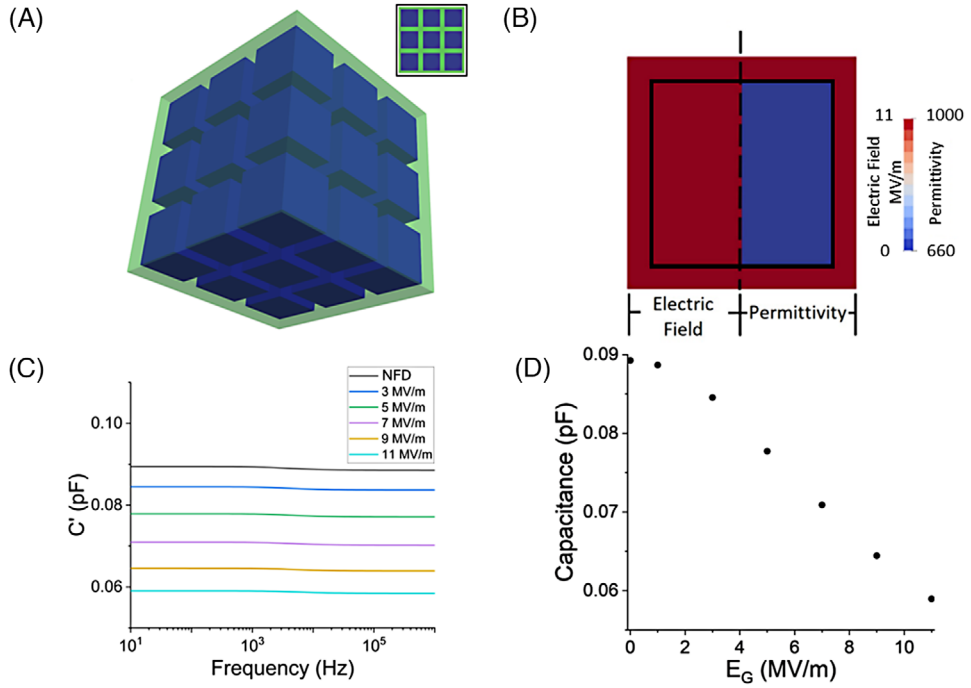

FIGURE 4 (A) Core–shell model used with the green shell region encapsulating the blue core region. Inset: A front-facing cut in half view of the respective model. (B) A combined view of the electric field (left) and final permittivity (right) for the center cube in the middle row for an E_G of 11 MV/m. The resulting electrical response in C' spectra is shown in (C) with the extracted capacitance (at 100 kHz) with increasing E_G shown in (D).

permittivity of $\varepsilon_r = 1000$ or 2000 and a conductivity of either $\sigma = 100$ or .1 μS/m. In Cases I–III, we simulate a field-dependent core, with a shell that is independent of the electric field, whereas in Cases IV–VI, we simulate conditions where both the core and shell are field dependent.

In Case I, we simulate a grain where the core and shell have the same conductivity of $\sigma = 100$ μS/m but the core has a higher permittivity of $\varepsilon_r = 2000$ compared to the shell with an initial value of $\varepsilon_r = 1000$. The core is only field dependent (i.e., $\beta = 1 \times 10^{10}$ Vm^5/C^3), whereas the shell is set with $\beta = 0$ Vm^5/C^3 making it field independent. As both the core and shell have the same conductivity, an E_G of 11 MV/m is generated throughout the core and shell material as shown in Figure 5A (left).

The electric field gives rise to a uniform drop in the core permittivity from its initial value of $\varepsilon_r = 2000$ to a value of 720, Figure 5A (right) when E_G reaches 11 MV/m. This results in the core permittivity dropping below that of the shell value of $\varepsilon_r = 1000$. In the C' spectra, Figure 5B for NFD, we initially observe two distinct plateaus at low electric fields of .134 pF (100 Hz) and .127 pf (100 kHz) representing the dominating components of the shell and core, respectively. As E_G is increased to 11 MV/m, the response becomes close to a single plateau with a measured capacitance of .077 pF, Figure 5C. This is a 40% drop from the NFD case and results in the permittivity at 100 kHz decreasing from an initial value of 1430 to 850 as shown in Figure 5D.

In Case II, we maintain the properties of the shell but reduce the core conductivity to $\sigma = 0.1$ μS/m. This now results in a model where the core is more resistive than the shell. The initial permittivity of the core is retained at $\varepsilon_r = 2000$ but as this region possesses lower conductivity, the electric field generated is now elevated compared to the shell as shown in Figure 6A (left). Again, note that the core is the only field-dependent material.

The field in the core is now no longer electrically homogeneous due to the more resistive core and this increased strength in the electric field in the core forms an "hourglass" shape leading to a greater drop in the permittivity of the core than in Case I, as shown in Figure 6A (right). The local electric field at the top and bottom regions of the core rises to 16 MV/m, dropping to a value of 14 MV/m nearer the center of the core. It should be noted that both these local values are higher than the applied E_G calculated by Equation (3) and highlight the importance of considering local electric fields.

Near the external regions of the core, the local field falls close to the global value of 11 MV/m due to the proximity of the conductive shell region and falls below the average within the top and bottom areas of shell material. As the permittivity change follows the electric field, the core, which starts with a single permittivity of $\varepsilon_r = 2000$,

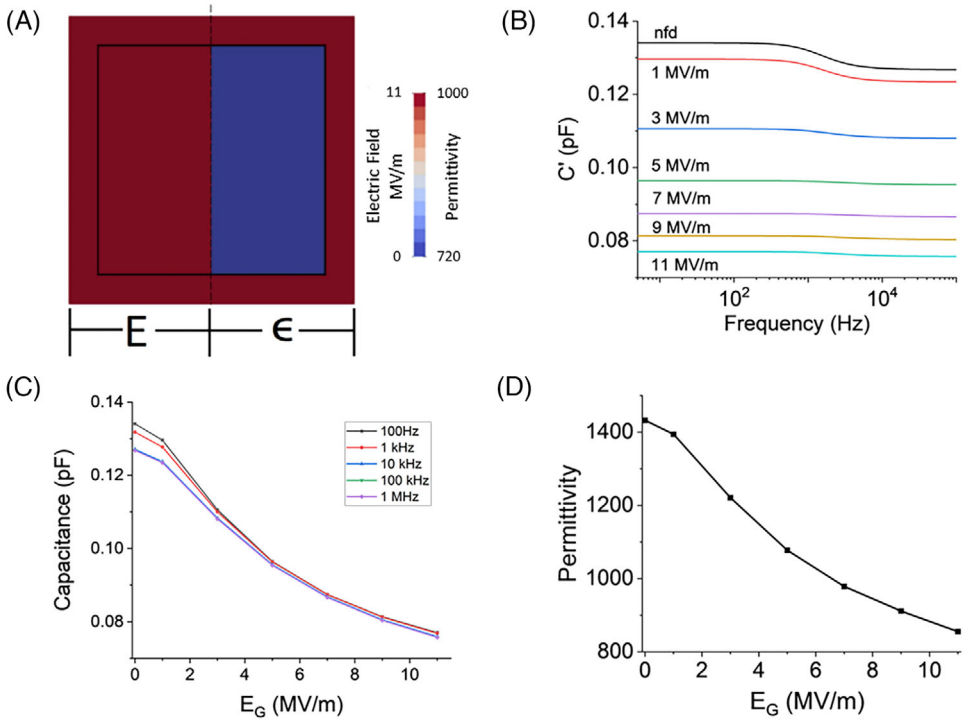

FIGURE 5 Case I, where both core and shell materials have the same conductivity. (A) Combined view of the electric field (left) and final permittivity (right) for an E_G of 11 MV/m. (B) Change in *C*' spectra as a function of global field, with extracted capacitance at various frequencies. (C) The change in capacitance as a function of E_G. A minimal change is observed with the curves overlapping at frequencies greater than 10 kHz. (D) Extracted permittivity (at 100 kHz) versus E_G.

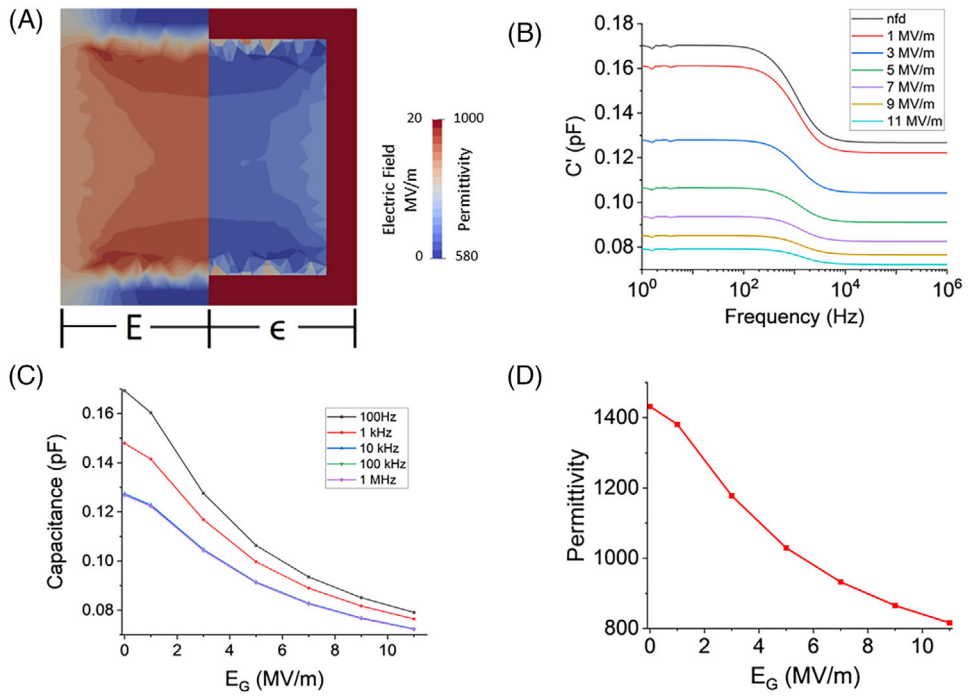

FIGURE 6 Case II, where the core material is more resistive than the shell material. (A) Combined view of the electric field (left) and final permittivity (right) for an E_G of 11 MV/m. (B) Change in *C*' spectra as a function of global field, with extracted capacitance at various frequencies. (C) The change in capacitance as a function of E_G. A minimal change is observed with the curves overlapping at frequencies greater than 10 kHz. (D) Extracted permittivity (at 100 kHz) versus E_G.

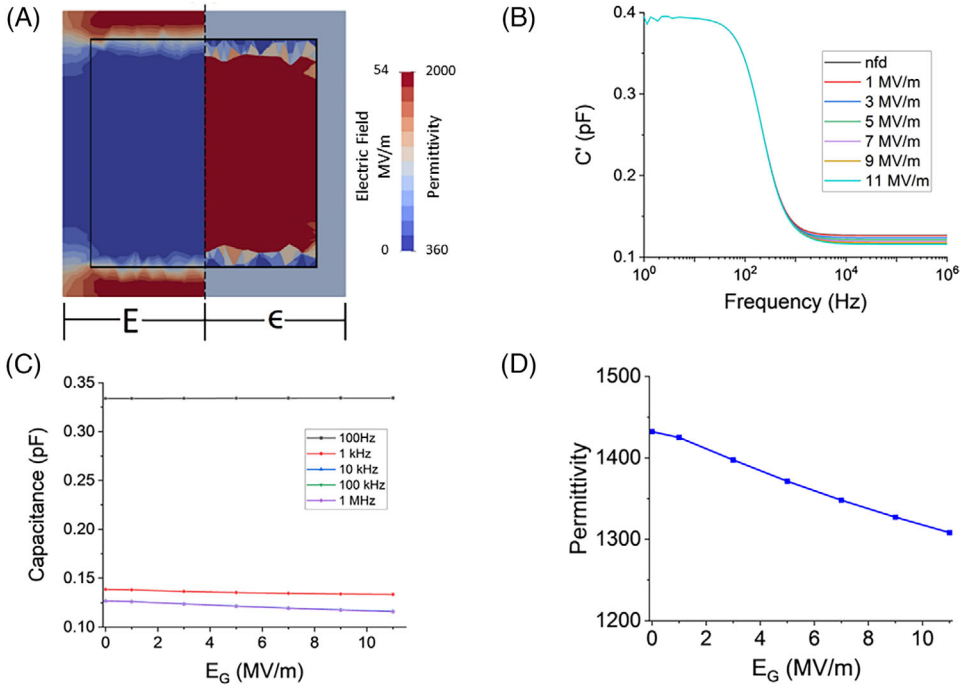

FIGURE 7 Case III, where the core material is more conductive than the shell material. (A) Combined view of the electric field (left) and final permittivity (right) for an E_G of 11 MV/m. (B) Change in C' spectra as a function of global field, with extracted capacitance at various frequencies. (C) The change in capacitance as a function of E_G. A minimal change is observed with the curves overlapping at frequencies greater than 10 kHz. (D) Extracted permittivity (at 100 kHz) versus E_G.

now becomes graded as it experiences a stronger reduction in the central regions than the edges. This leads to over half the core's volume, which consists of the top, bottom, and central regions, dropping to a permittivity value of $500 < \varepsilon_r < 650$, whereas the remainder of the core volume reduces to $650 < \varepsilon_r < 950$. As a consequence, the resulting C' spectra and permittivity Figure 6C,D show a strong change as a function of the field. For the NFD case, there are two distinct plateaus in C' of .170 and .127 pF, Figure 6C. As the global field strength is increased to 11 MV/m, the capacitance response for the shell- and core-dominated regions both drop to values of .078 and .071 pF, respectively. Additionally, the difference in capacitance between the shell and the core drops from .043 pF for the NFD case, to a difference of just .005 pF for an E_G of 11 MV/m. The effective permittivity at 100 kHz also drops to nearly half, with the high field case $\varepsilon_r = 800$ compared to the NFD simulation of $\varepsilon_r = 1430$. As the electric field is increased, the permittivity of the core is also reduced below that of the shell, bringing plateaus in C' spectra closer together.

In Case III, we reverse the conductivity of Case II thereby making the core more conductive than the shell. Consequently, the electric field experienced in the core falls below the global field value of 11 MV/m, as shown in Figure 7A (left). The shell regions above and below the core region account for ~10% of the grain volume and experiences an extremely high field of ~54 MV/m but this drops sharply to .80 MV/m in the regions to the side of the core. This reduction in the electric field leaves a large amount of the core, over 80%, relatively unchanged from the initial value of $\varepsilon_r = 2000$. This illustrates that the shell, while under an enhanced electric field, provides a shielding effect to the core and therefore reduces the electric field that it experiences.

As shown in Figure 7B, the high-frequency plateau arising predominantly from the core response experiences a low field-dependent change. At NFD, C' is .138 pF at 100 kHz and when a global field of 11 MV/m is applied, the high-frequency C' plateau falls by only 8% to .127 pF. The low-frequency plateau, associated predominantly with the shell, remains unchanged at .397 pF as shown in Figure 7B. As a consequence, the permittivity drops from its initial value of $\varepsilon_r = 1430$ to 1310, Figure 7D. Unlike the previous cases, Case III still exhibits a clear core–shell response even after a field is applied.

We now move on to cases where both materials are ferroelectric and exhibit field dependence. Here, we use the material configurations of Cases I, II, and III but assign both the core and shell $\beta = 1.0 \times 10^{10}$ Vm^5/C^3.

In Case IV, as in Case I, the core and shell are assigned a conductivity of $\sigma = 100$ μS/m. The core is assigned a higher permittivity of $\varepsilon_r = 2000$ compared to the shell with an initial value of $\varepsilon_r = 1000$. Due to the shell and core having the same conductivity, we once again observe an E_G of

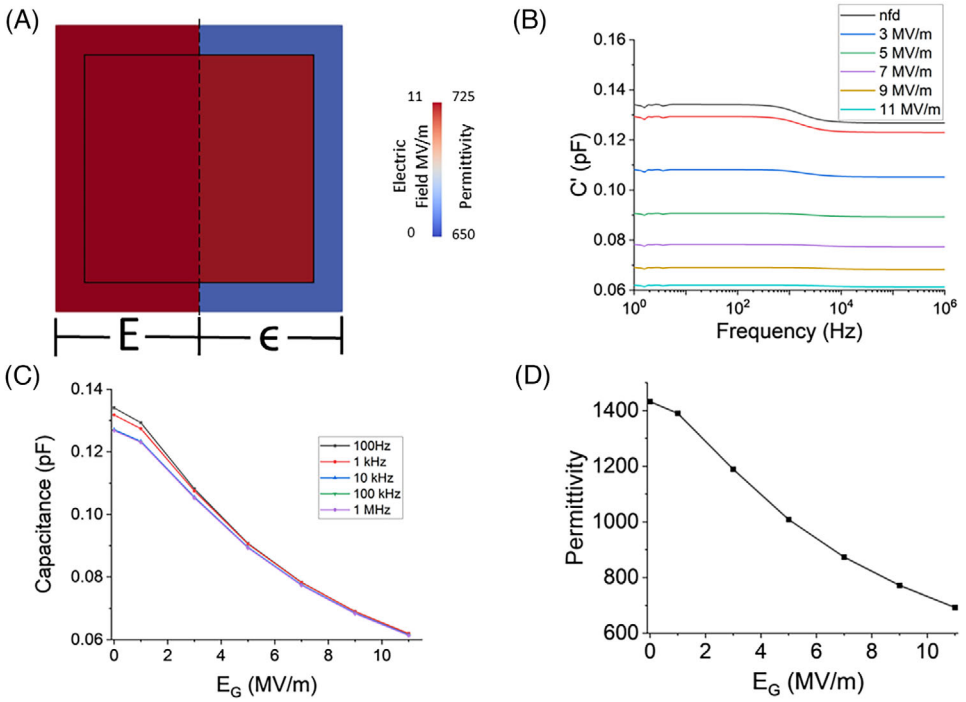

FIGURE 8 Case IV, where both core and shell materials have the same conductivity. (A) Combined view of the electric field (left) and final permittivity (right) for an E_G of 11 MV/m. (B) Change in C' spectra as a function of global field, with extracted capacitance at various frequencies. (C) The change in capacitance as a function of E_G. A minimal change is observed with the curves overlapping at frequencies greater than 10 kHz. (D) Extracted permittivity (at 100 kHz) versus E_G.

11 MV/m generated throughout the core and shell materials as shown in Figure 8A (left). This electric field leads to a uniform drop in the core from an initial value of ε_r from 2000 to 720, Figure 8A (right), similar to that of Case I. However, the shell now also experiences a drop in ε_r from 1000 to 650 and as a consequence the core permittivity remains higher than that of the shell as E_G is increased.

In the C' spectra, Figure 8B for NFD, we initially observe two distinct plateaus at low electric fields of .134 pF (100 Hz) and .127 pf (100 kHz) representing the dominating components of the shell and core, respectively. As E_G is increased to 11 MV/m, the response becomes close to a single plateau with a measured capacitance of .062 pF, Figure 8C. This results in a 52% drop from the NFD case and permittivity at 100 kHz decreasing from an initial value of 1430 to 700, as shown in Figure 8D.

As in Case II, in Case V, the core conductivity is set as $\sigma = .1$ μS/m, lower than that of the shell with $\sigma = 100$ μS/m resulting in a resistive shell model. Again, note that in this case, both materials are field dependent. As in Case II, the electric field in the core is now no longer electrically homogeneous, Figure 9A (left) and forms an "hourglass" shape. This leads to a greater drop in the permittivity of the core than in Case II, as shown in Figure 9A (right). The local electric field at the top and bottom regions of the core rises to 16 MV/m dropping to a value of 14 MV/m nearer the center of the core, now higher than the value of the global field. Toward the core–shell interface, the local field is close to the global value of 11 MV/m and then falls below the average within the top and bottom areas of the shell material. The permittivity of the core once again becomes graded with over half the core's volume, dropping to a permittivity value of $500 < \varepsilon_r < 650$, whereas the rest of the core volume reduces to $650 < \varepsilon_r < 950$. In the shell region, as the local electric field at the top and bottom of the core is low, a negligible drop in the permittivity of the shell in this area is generated. However, in the regions surrounding the side of the core, the field is elevated to 12 MV/m leading to a permittivity drop in the shell to a value of approximately $\varepsilon_r = 650$.

This response results in C' spectra and permittivity Figure 9C,D showing a stronger change as a function of field than in Case II. For the NFD case, there are two distinct plateaus in C' of .170 and .127 pF, Figure 6C. As E_G is increased to 11 MV/m, the capacitance response for the shell- and core-dominated regions both drops to values of .067 and .060 pF, respectively. Additionally, the difference in capacitance between the shell and the core drops from .043 pF for the NFD case, to a difference of just .007 pF for an E_G of 11 MV/m. The effective permittivity at 100 kHz also drops to over half, with the high field case $\varepsilon_r = 680$ compared to the NFD simulation of $\varepsilon_r = 1430$. As the

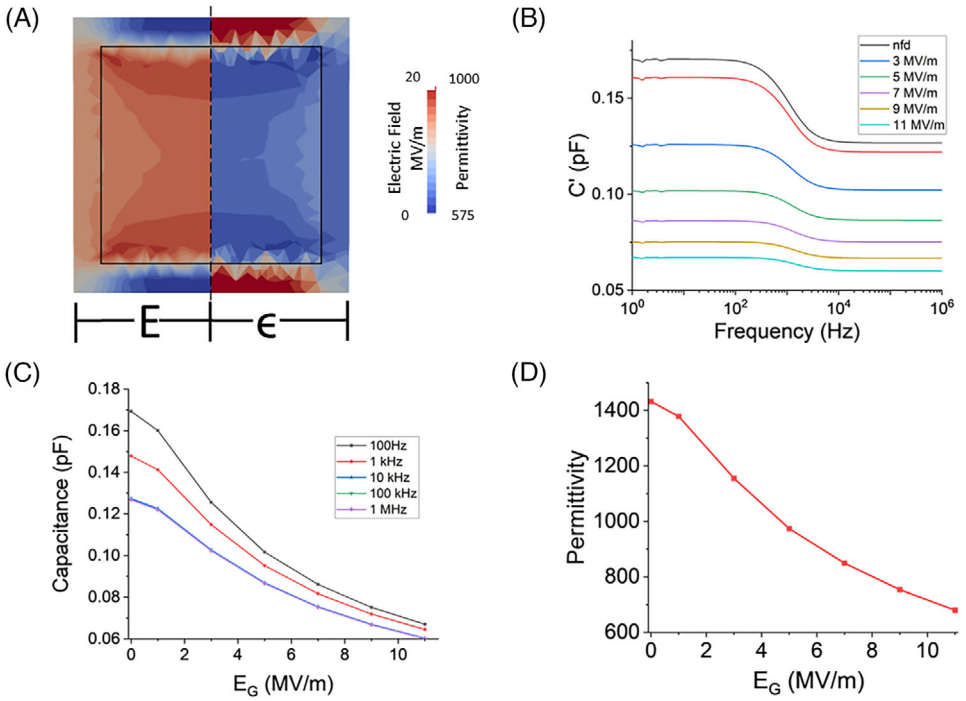

FIGURE 9 Case V, where the core material is more resistive than the shell material. (A) Combined view of the electric field (left) and final permittivity (right) for an E_G of 11 MV/m. (B) Change in C' spectra as a function of global field, with extracted capacitance at various frequencies. (C) The change in capacitance as a function of E_G. A minimal change is observed with the curves overlapping at frequencies greater than 10 kHz. (D) Extracted permittivity (at 100 kHz) versus E_G.

electric field is increased, the low-frequency response drops more rapidly than that of the high-frequency response, bringing the plateaus in C' spectra closer together.

In Case VI, we reverse the conductivity of Case V, and the core is now more conductive than the shell. Consequently, just as in Case III, the electric field experienced in the core falls below the global field value of 11 MV/m, Figure 10A (left). The shell regions above and below the core experience an extremely high field of ~54 MV/m dropping sharply to .90 MV/m in the regions surrounding the side of the core. As simulated in Case III, it leaves over 80% of the core unchanged from its initial value of $\varepsilon_r = 2000$. Crucially, however, as the shell is now field dependent, due to the high field in the top and bottom regions of the shell, the permittivity in these regions drops dramatically from the initial value of $\varepsilon_r = 2000$ to below 400, leading to a greater significant change overall.

As shown in Figure 10B, at NFD, C' is .127 pF at 100 kHz and when a global field of 11 MV/m is applied, the high-frequency C' plateau falls by only 45.8% to .0688 pF. The low-frequency plateau, associated predominantly with the shell, decreases by 65% from .334 pF to .117 pF as shown in Figure 10C. This leads to a drop in permittivity from its initial value of $\varepsilon_r = 1430$ to 780, Figure 10D. Unlike Cases IV and V, Case VI still exhibits a clear core–shell response even after a field is applied.

Comparing all permittivity drops at 100 kHz, in Figure 11, we see that all cases, except for Case III, follow a trend similar to that shown in Figure 1. Both experimental and model data experience a decrease in permittivity of about 40%–50% at an E_G of ~10 MV/m.

These studies show that a key parameter in determining the core material change is the surrounding material's conductivity. As shown in Figure 11A, Cases I and II show significant sensitivity to the global electric field if the core material is lower or equal in conductivity to that of the shell. In Case I, the conductivity of the materials is identical and as such the electric field set up in both materials is the same (Figure 5A). This leads to the system responding with a permittivity change in the core due to the applied global field. In Case II, as the conductivity of the core is lower than the shell, an enhanced current density is generated in the core region (Figure 6A), consistent with work shown by Heath et al.[35] This leads to an enhanced electric field in the core and as such greater VCC sensitivity. In these configurations, it offers the ability to tune the capacitance and as such TCC through the control of dielectric layer thickness. This could be detrimental, however, as the increased local electric field could raise the likelihood of the core material failing and the possibility of dielectric breakdown. While Cases IV and V have the same material properties as Cases I and II, although the shell is now field sensitive they still behave similarly. In Case IV,

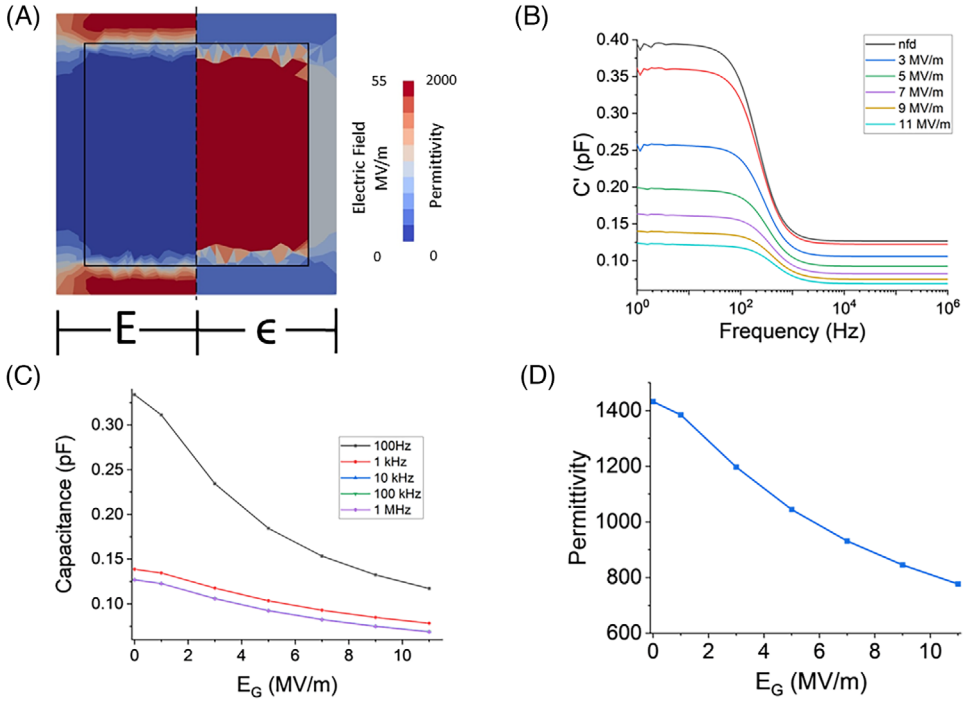

FIGURE 10 Case VI, where the core material is more conductive than the shell material. (A) Combined view of the electric field (left) and final permittivity (right) for an E_G of 11 MV/m. (B) Change in C' spectra as a function of global field. (C) Capacitance extracted at various fixed frequencies versus E_G. There is minimal change in capacitance and the curves overlap at frequencies greater than 10 kHz. (D) Extracted permittivity (at 100 kHz) versus E_G.

FIGURE 11 (A) The overall decrease in permittivity for each case versus E_G. Data sets with the same color have the same material properties except for the field dependency of the shell. Cases I and II are highly field dependent, whereas it is much less pronounced in Case III. Cases IV, V, and VI all experience a higher field dependency than Cases I, II, and III. (B) Normalized permittivity versus field plot comparing the experimental data to Cases IV, V, and VI.

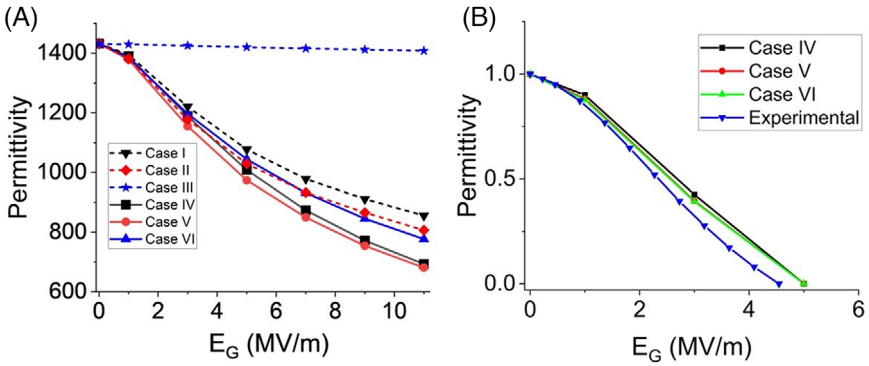

where the materials have the same conductivity, the shell VCC response now causes the overall permittivity to drop, which can be seen in Figure 11A. This is also true of Case II but with a reduced amount due to the current mostly acting through the core and avoiding, if possible, the more resistive parallel shell regions lowering the electric field in those regions (Figure 6A).

If the core is surrounded by a lower conductive material, such as Case III, the current primarily wants to find the path of least resistance through the core. This generates a higher electric field in the shell material, primarily in the top and bottom layers, as seen in Figure 10A. This effectively "screens" the core from high local electric fields causing the system to exhibit almost little or no NFD. Only a small region of the model, primarily the top and bottom surfaces of the core, experiences a high local field whereas the rest of the core material remains unchanged. This leads to the capacitance remaining relatively constant when increasing the global electric field and therefore reducing the system's apparent sensitivity to field effects. If the shell material is assigned field dependence as in Case VI, while the shielding effect to the core is still present, the shell material now experiences a drop in permittivity instead. Although this drop in Case VI is much stronger than in Case III, it is still less than that experienced by Cases IV and V. In Figure 11B, it can be seen that after normalizing the plot for permittivity, all plots, regardless of their VCC strength, they all experience the same

general trend. It also shows that the experimental data follow a similar rate of drop in permittivity as the model data for Cases IV, V, and VI as the voltage is increased to 5 MV/m.

The studies shown here investigate how large changes in permittivity and conductivity of those regions affect the response; however, small changes (~10% variation) in either the core or shell conductivity caused less than a 5% change in the overall field dependence response. It is only when the values start to become comparable (less than two orders of magnitude) that the current paths through the system are altered and then begin to affect the observed field dependence. We note, however, that the changes to the β value do influence the response more significantly, mainly as it is a scaling component of Equation (4), but the trend of the models, irrespective of the value used, remains the same.

Through the models presented here, we have assigned a 50:50 volume ratio for the core and shell materials. The measured strength of the VCC dependence of the system will be modified by the core–shell volume ratio due to changes in the current and field profiles previously shown by Heath et al.[34] For example, if the volume fraction of core material were made larger and more conductive, a greater flow of current through the core would be expected, thereby raising the electric field. This would lead to a lower shielding effect and a greater field dependence to be exhibited. Other effects present in MLCC materials, such as grain shape,[28] roughness,[35] or porosity,[36] have been shown to increase local electric fields and along with volume fraction are the focus of on-going and future studies.

In conclusion, we have developed a finite element modelling approach that can aid the understanding of how VCC is affected by the electric microstructure of a system. Typically, MLCC materials are formed from a $BaTiO_3$ material with a doped shell, giving rise to a core that has higher conductivity than the surrounding shell. The findings in this article indicate in this case over 80% of the core volume experiences a field that is lower than the global value applied and as such the core response is relatively unchanged. If the shell has little or NFD, then the apparent VCC change is negligible (Figure 11A, blue stars); however, if the shell does possess some field dependence, although the field which the core experiences is still reduced, a VCC reduction is observed (Figure 11A, blue triangles) and attributed to the change in the properties of the shell. Therefore, through a selection of the core and shell properties, the VCC effects can be enhanced or suppressed as desired while still shielding the core from the high electric fields and improving the apparent breakdown strength of the system. These simulations provide an improved understanding of voltage dependence and help guide the design of future materials for MLCCs with improved performance.

ACKNOWLEDGMENTS

The authors have nothing to report.

ORCID

Rassell C. D'Silva Green https://orcid.org/0009-0007-5463-6708
Julian S. Dean https://orcid.org/0000-0001-7234-1822

REFERENCES

1. Analysis of global multi-layer ceramic capacitor (MLCC) markets, 2019–2024. ResearchAndMarkets.com. 2019. [cited 2023 June 7]. Available from: https://www.businesswire.com/news/home/20191209005389/en/Analysis-of-Global-Multi-Layer-Ceramic-Capacitor-MLCC-Markets-2019-2024—ResearchAndMarkets.com
2. Sun Y, Wu S, Zhang J, Hwang C, Yang Z. Measurement methodologies for acoustic noise induced by multilayer ceramic capacitors of power distribution network in mobile systems. IEEE Trans Electromagn Compat. 2020;62(4):1515–23. https://doi.org/10.1109/TEMC.2020.2993850
3. Abebe R, Vakil G, Calzo GL, Cox T, Lambert S, Johnson M, et al. Integrated motor drives: state of the art and future trends. IET Electr Power Appl. 2016;10(8):757–71. https://doi.org/10.1049/iet-epa.2015.0506
4. Kerridge G, Sinclair DC, Dean JS. Resource efficient exploration of ternary phase space to develop multi-layer ceramic capacitors. Acta Mater. 2021;207:116690. https://doi.org/10.1016/j.actamat.2021.116690
5. Hoshina T, Takizawa K, Li J, Kasama T, Kakemoto H, Tsurumi T. Domain size effect on dielectric properties of barium titanate ceramics. Jpn J Appl Phys. 2008;47(9 PART 2):7607–11. https://doi.org/10.1143/JJAP.47.7607
6. Hong K, Lee TH, Suh JM, Yoon SH, Jang HW. Perspectives and challenges in multilayer ceramic capacitors for next generation electronics. J Mater Chem C Mater. 2019;7(32):9782–802. https://doi.org/10.1039/c9tc02921d
7. Pan MJ, Randall C. A brief introduction to ceramic capacitors. IEEE Electrical Insul Mag. 2010;26(3):44–50. https://doi.org/10.1109/MEI.2010.5482787
8. Jeon SC, Yoon BK, Kim KH, Kang SJL. Effects of core/shell volumetric ratio on the dielectric-temperature behavior of $BaTiO_3$. J Adv Ceram. 2014;3(1):76–82. https://doi.org/10.1007/s40145-014-0096-y
9. Gong H, Wang X, Zhang S, Li L. Synergistic effect of rare-earth elements on the dielectric properties and reliability of $BaTiO_3$-based ceramics for multilayer ceramic capacitors. Mater Res Bull. 2016;73:233–39. https://doi.org/10.1016/j.materresbull.2015.07.010
10. Park KJ, Kim CH, Yoon YJ, Song SM, Kim YT, Hur KH. Doping behaviors of dysprosium, yttrium and holmium in $BaTiO_3$ ceramics. J Eur Ceram Soc. 2009;29(9):1735–41. https://doi.org/10.1016/j.jeurceramsoc.2008.10.021
11. Benlahrache MT, Benhamla N, Achour S. Dielectric properties of $BaTiO_3$–$NaNbO_3$ composites. J Eur Ceram Soc.

2004;24(6):1493–96. https://doi.org/10.1016/S0955-2219(03)00577-6

12. Wang SF, Dayton GO. Dielectric properties of fine-grained barium titanate based X7R materials. J Am Ceram Soc. 1999;82(10):2677–82. https://doi.org/10.1111/j.1151-2916.1999.tb02141.x
13. Arlt G, Hennings D, De With G. Dielectric properties of fine-grained barium titanate ceramics. J Appl Phys. 1985;58(4):1619–25. https://doi.org/10.1063/1.336051
14. Padurariu L, Curecheriu L, Buscaglia V, Mitoseriu L. Field-dependent permittivity in nanostructured $BaTiO_3$ ceramics: modeling and experimental verification. Phys Rev B Condens Matter Mater Phys. 2012;85(22):1–9. https://doi.org/10.1103/PhysRevB.85.224111
15. Yue Z, Zhao J, Yang G, Li L. Electric field-dependent properties of $BaTiO_3$-based multilayer ceramic capacitors. Ferroelectrics. 2010;401:56–60. https://doi.org/10.1080/00150191003670424
16. Wei X, Yao X. Analysis on dielectric response of polar nanoregions in paraelectric phase of relaxor ferroelectrics. J Appl Phys. 2006;100(6):64319. https://doi.org/10.1063/1.2337408/370305
17. Deluca M, Stoleriu L, Curecheriu LP, Horchidan N, Ianculescu AC, Galassi C, et al. High-field dielectric properties and Raman spectroscopic investigation of the ferroelectric-to-relaxor crossover in $BaSn_xTi_{1-x}O_3$ ceramics. J Appl Phys. 2012;111(8):84102. https://doi.org/10.1063/1.3703672
18. Johnson KM. Variation of dielectric constant with voltage in ferroelectrics and its application to parametric devices. J Appl Phys. 1962;33(9):2826–31. https://doi.org/10.1063/1.1702558
19. Placeres Jiménez R, Pedro Rino J, Marino Gonçalves A, Antonio Eiras J. Nonlinear dielectric response and transient current: an effective potential for ferroelectric domain wall displacement. Appl Phys Lett. 2013;103(11):112901. https://doi.org/10.1063/1.4820589/130034
20. Curecheriu LP, Mitoseriu L, Ianculescu A. Nonlinear dielectric properties of $Ba_{1-x}Sr_xTiO_3$ ceramics. J Alloys Compd. 2009;482(1–2):1–4. https://doi.org/10.1016/j.jallcom.2009.04.036
21. Wei X, Feng Y, Hang L, Yao X. Dielectric properties of barium stannate titanate ceramics under bias field. Ceram Int. 2004;30:1401–4. https://doi.org/10.1016/j.ceramint.2003.12.084
22. Curecheriu LP, Tufesclt FM, Ianculescu A, Ciomaga CE, Mitoseriu L, Stancu A. Tunability characteristics of $BaTiO_3$-based ceramics: modeling and experimental study. J Optoelectron Adv Mater. 2008;10:1792–95. https://doi.org/10.2298/PAC0702023C
23. Curecheriu L, Buscaglia MT, Buscaglia V, Zhao Z, Mitoseriu L. Grain size effect on the nonlinear dielectric properties of barium titanate ceramics. Appl Phys Lett. 2010;97(24):242909–242909-3. https://doi.org/10.1063/1.3526375
24. Myroshnychenko V, Smirnov S, Mulavarickal Jose PM, Brosseau C, Förstner J. Nonlinear dielectric properties of random paraelectric-dielectric composites. Acta Mater. 2021;203:116432. https://doi.org/10.1016/j.actamat.2020.10.051
25. Liou JW, Chiou BS. Analysis of the dielectric characteristics for polycrystalline $Ba_{0.65}Sr_{0.35}TiO_3$ (II)—d.c. Field dependence with a modified bias equation. J Mater Sci: Mater Electron. 2000;11(8):645–51. https://doi.org/10.1023/A:1008949316917
26. Zhang G, Jiang S, Zeng Y, Zhang Y, Zhang Q, Yu Y. The modified model of the dielectric characteristics for porous $Ba_{0.6}Sr_{0.4}TiO_3$ ceramics. J Appl Phys. 2009;106(3):034110. https://doi.org/10.1063/1.3183921
27. Zhao Z, Buscaglia V, Viviani M, Buscaglia MT, Mitoseriu L, Testino A, et al. Grain-size effects on the ferroelectric behavior of dense nanocrystalline $BaTiO_3$ ceramics. Phys Rev B Condens Matter Mater Phys. 2004;70(2):024107. https://doi.org/10.1103/PhysRevB.70.024107
28. Dean JS, Harding JH, Sinclair DC. Simulation of impedance spectra for a full three-dimensional ceramic microstructure using a finite element model. J Am Ceram Soc. 2014;97(3):885–91. https://doi.org/10.1111/jace.12750
29. Geuzaine C, Remacle JF. Gmsh. Published online 2022.
30. Heath JP, Harding JH, Sinclair DC, Dean JS. The analysis of impedance spectra for core-shell microstructures: why a multiformalism approach is essential. Adv Funct Mater. 2019;29(38):1904036. https://doi.org/10.1002/adfm.201904036
31. Hennings D, Rosenstein G. Temperature-stable dielectrics based on chemically inhomogeneous $BaTiO_3$. J Am Ceram Soc. 1984;67(4):249–54. https://doi.org/10.1111/J.1151-2916.1984.TB18841.X
32. Zhao C, Zhang H, Yang L, Wang Y, Ding Y. Dual laser beam revising the separation path technology of laser-induced thermal-crack propagation for asymmetric linear cutting glass. Int J Mach Tools Manuf. 2016;106:43–55. https://doi.org/10.1016/j.ijmachtools.2016.04.005
33. Buscaglia MT, Viviani M, Buscaglia V, Mitoseriu L, Testino A, Nanni P, et al. High dielectric constant and frozen macroscopic polarization in dense nanocrystalline $BaTiO_3$ ceramics. Phys Rev B Condens Matter Mater Phys. 2006;73(6):064114. https://doi.org/10.1103/PHYSREVB.73.064114/FIGURES/6/MEDIUM
34. Heath JP, Dean JS, Harding JH, Sinclair DCJ. Simulation of impedance spectra for core-shell grain structures using finite element modelling. J Am Ceram Soc. 2015;98(6):1925–31. https://doi.org/10.1111/JACE.13533
35. Heath JP, Dean JS, Harding JH, Sinclair DCJ. Electric field enhancement in ceramic capacitors due to interface amplitude roughness. J Am Ceram Soc. 2019;39(4):1170–77. https://doi.org/10.1016/j.jeurceramsoc.2018.10.033
36. Dale G, Strawhorne M, Sinclair DCJ, Dean JS. Finite element modelling on the effect of intra-granular porosity on the dielectric properties of $BaTiO_3$ MLCCs. J Am Ceram Soc. 2017;101(3):1211–20. https://doi.org/10.1111/jace.15261

How to cite this article: D'Silva Green RC, Dale G, McLaughlin G, Strawhorne M, Sinclair DC, Dean JS. Application of Johnson's approximation in finite element modeling for electric field-dependent materials. Int J Appl Ceram Technol. 2024;1–13. https://doi.org/10.1111/ijac.14824